Supporting Information (SI)

Significant Enhancement of Visible Light-Driven Hydrogen Evolution by Structure Regulation of Carbon Nitrides

Qing Han[*]*, Zhihua Cheng, Bing Wang, Huiming Zhang*[*]*and Liangti Qu*[*]

Key Laboratory of Photoelectronic/Eletrophotonic Conversion Materials, Key Laboratory of Cluster Science, Ministry of Education of China, School of Chemistry and Chemical Engineering, Beijing Institute of Technology, Beijing 100081, P. R. China.

[*]Email: qhan@bit.edu.cn; huimin@bit.edu.cn; lqu@bit.edu.cn

This supporting information file includes:

PART I: EXPERIMENTAL SECTION

Photochemical measurement. Wavelength dependence of H_2 evolution rate was measured by using appropriate band pass filters (400, 420, 450, 500 and 550 nm, respectively) to perform the water splitting experiment under the designated monochromic light. The intensity of the monochromic light was averaged at 13 representative points by CEL-NP 2000 Photoradiometer and the active area of the reactor was approximately 38.5 cm^2. The external quantum yield was then calculated by the following Equation (1):

$$\Phi = \frac{2 \times \text{amount of } H_2 \text{ molecules evovled}}{\text{number of incident photons}} \times 100 \qquad (1)$$

The turnover number (TON) was estimated by the following Equation (2):

$$\text{TON} = \frac{\text{moles of } H_2 \text{ molecules evovled}}{\text{moles of platinum on the photocatalyst}} \qquad (2)$$

PARPT II: SUPPORTED FIGURES

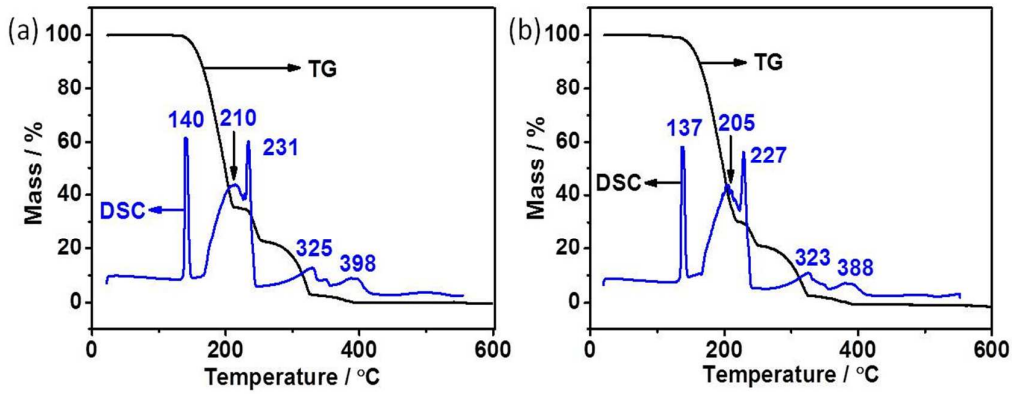

Figure S1. Thermogravimetric-differential scanning calorimetry (TG-DSC) thermograms of (a) pristine urea and (b) SRU-100.

Comparing with pristine urea (Figure S1a), TG-DSC analysis (Figure S1b) of SRU-100 shows decrease in temperature at the melting point (137 ^{o}C vs. 140 ^{o}C), the reaction of urea to cyanamide (205 ^{o}C vs. 210 ^{o}C), the thermal condensation of cyanamide into melamine (227 ^{o}C vs. 231 ^{o}C), the further condensation of melamine into melem (323 ^{o}C vs. 325 ^{o}C), and the formation of carbon nitride (388 ^{o}C vs. 398 ^{o}C), respectively. This result indicates the decreased precursor size leads to decreased temperature of the thermal polycondensation and evaporation.

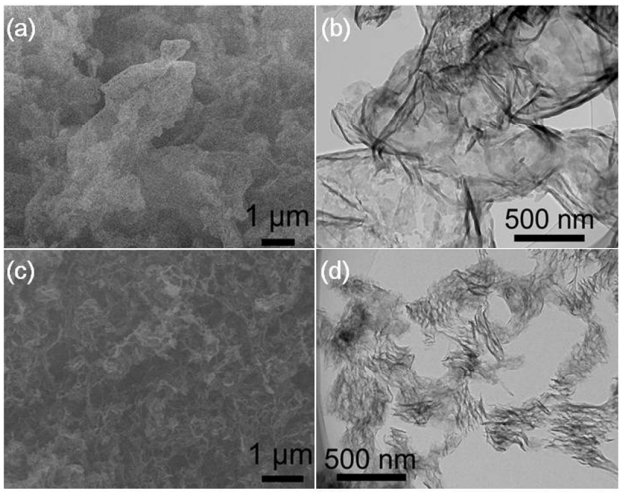

Figure S2. (a) SEM, (b) TEM of GCN; (c) SEM, (d) TEM of DACN-100.

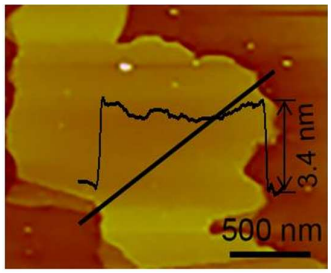

Figure S3. AFM images of DACN-100 and its height profile along the line.

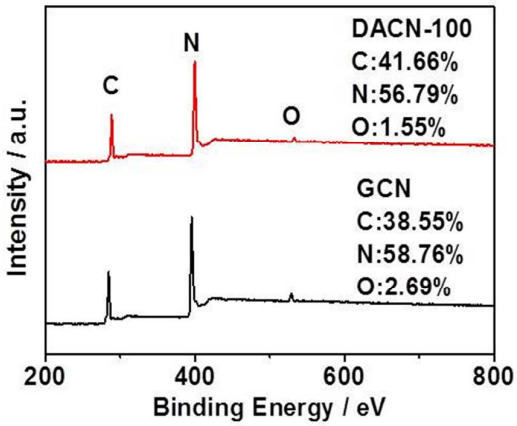

Figure S4. XPS spectra of GCN and DACN-100.

Table S1. The element content (at%) of GCN, DACN-100 determined by XPS.

Sample	C	N	O	C/N
GCN	**38.55**	**58.76**	**2.69**	**0.66**
DACN-100	**41.66**	**56.79**	**1.55**	**0.73**

Table S2. The relative percentages (at%) of the nitrogen and carbon species for GCN and DACN-100 obtained from XPS.

Sample	N_{2C}	N_{3C}	N-NH_x	$(N_2)C(NH_2)$	C-C
GCN	**63.2**	**25.9**	**10.9**	**83.2**	**16.8**
DACN-100	**71.3**	**20.9**	**7.8**	**92.2**	**7.8**

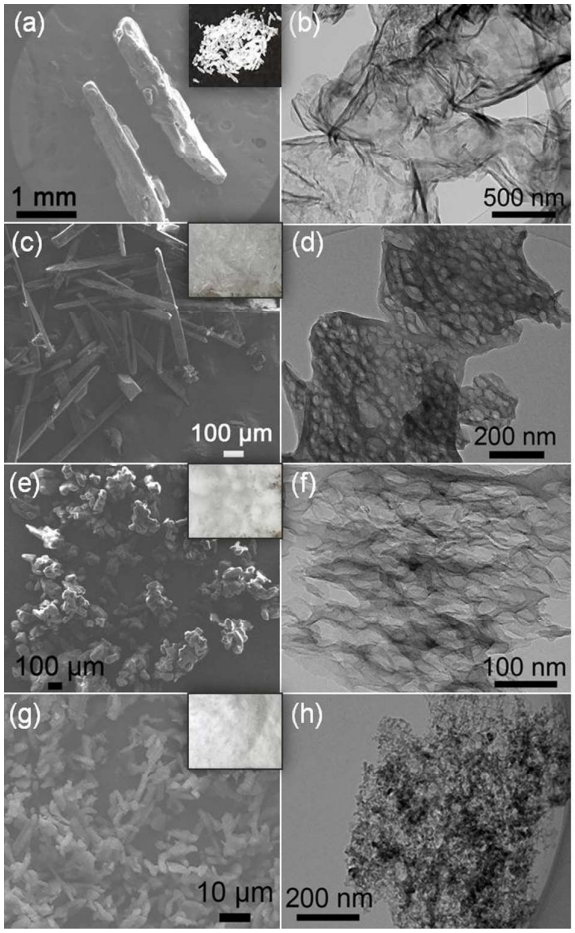

Figure S5. SEM images and Photographs (insets) of a) pristine urea, c) SRU-500, e) SRU-100 and g) SRU-10 and the corresponding TEM images of b) GCN, d) DACN-500, f) DACN-100 and h) DACN-10.

As shown in Figure S5, the pristine urea (Figure S5a) was altered to microcrystals of 500 μm (SRU-500, Figure S5c) and 10 μm (SRU-10, Figure S5g) under different conditions. The DACN samples obtained by calcination of SRU-500 and SRU-10 at 600 ºC are notated as DACN-500 and DACN-10, respectively. TEM images reveal that the DACN-500 (Figure S5d) becomes rougher with respect to GCN (Figure S5b) and is enriched with aligned pores in range of 20-50 nm, suggesting the disruption of the long-range atomic order of two-dimension GCN in both perpendicular and parallel directions. The DACN-100 (Figure S5f) shows greater disorder than DACN-500 (Figure S5d) in which collapse of partial pore walls in one orientation of DACN-500. Further decrease of precursor grain size led to the formation of agglomerate fragments around 10 nm in size (DACN-10, Figure S5h). These speak for the degree of disorder in the atomic arrangement in carbon nitride materials increases with the reduction of precursor grain size.

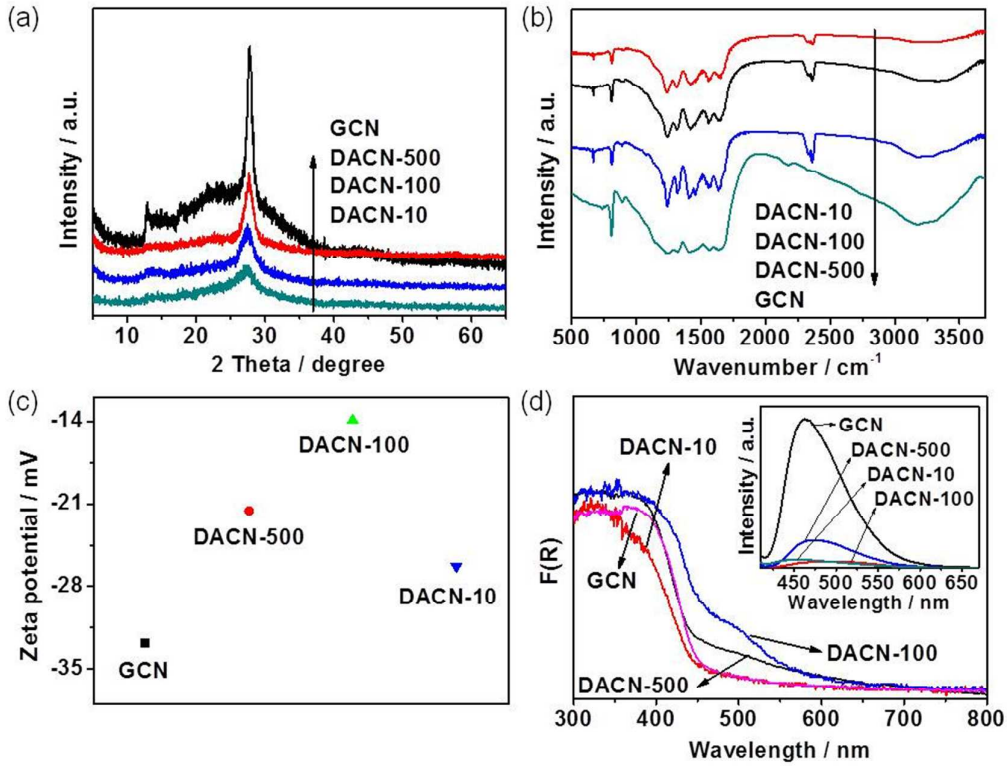

Figure S6. (a) XRD patterns, (b) FT-IR spectra, (c) Ratios of bonds within N1s core-level peak in different samples and (d) UV/Vis diffuse reflectance spectra (Inset: PL spectra) of GCN, DACN-500, DACN-100 and DACN-10.

As the particle size decreases, both the 13.0° and 27.7° peaks of DACN samples gradually weakened, as well as a downshift from 27.7° for GCN to 27.5° for DACN-500 and 27.3° for DACN-10 (Figure S6a), demonstrating gradually enhance destruction of in-plane and interlayer periodic structure as observed in TEM images (Figure S5). IR spectra (Figure S6b) reveal the DACN display gradual weakening N-H stretching peaks between 2900 and 3340 cm^{-1}, demonstrating an increased loss of nitrogen atoms with the enhanced short-range structure. The C/N ratios increase from 3:4.6 (GCN) to 3:4.5 (DACN-500), 3:4.1 (DACN-100) and 3:2.2 (DACN-10), respectively (Figure S7a, Table S3, S4), further illustrating more and more severe loss of nitrogen atom. XPS spectra in N1s (Figure S7b, Figure S6c) show the percentage of N-H_x decrease from 10.9 at% in GCN to 9.1 at% in DACN-500, 7.8 at% in DACN-100, implying decline in amino groups with the disrupted long-range atomic

order. As a consequence of the loss of N-H_x atoms, the ratio of $N_{2C}/(N_{3C}+N\text{-}H_x)$ increases from 1.7 (GCN) to 2.2 (DACN-500), and reaches to a maximum of 2.5 for VACN-100. However, a further decrease of precursor size causes more amino groups (the content of N-H_x is 9.7 at% for DACN-10), and leads to a dramatic decrease in the ratio of $N_{2C}/(N_{3C}+N\text{-}H_x)$ (1.9 for DACN-10). These results illustrate gradual removing of a portion of amine groups with reduction of urea sizes. A further decrease of urea size leads to increase in amino groups and decrease in sp^2 C-N=C bonds of DACN-10 possibly because of the cleavage of the C-N bonds during the thermal treatment. Further, the intensity of $(N_2)C(NH_2)$ increases (Figure S8, Table S4), and zeta potential decreases (inset in Figure S6c), strong evidence that NH_x vacancies were gradually introduced into GCN. The redshift and blueshift in absorption edge was achieved for DACN-500 (475 nm) and DACN-10 (448 nm, Figure S6d), respectively, which should be attributed to the existence of holes and the quantum confinement effect.[s1] These redshift and blueshift can be also observed in the PL spectra of DACN-500 and DACN-10. In addition, the PL is gradually quenched for DACN samples with the urea size decrease, indicating that the changes in surface NH_x vacancies can improve charge separation.

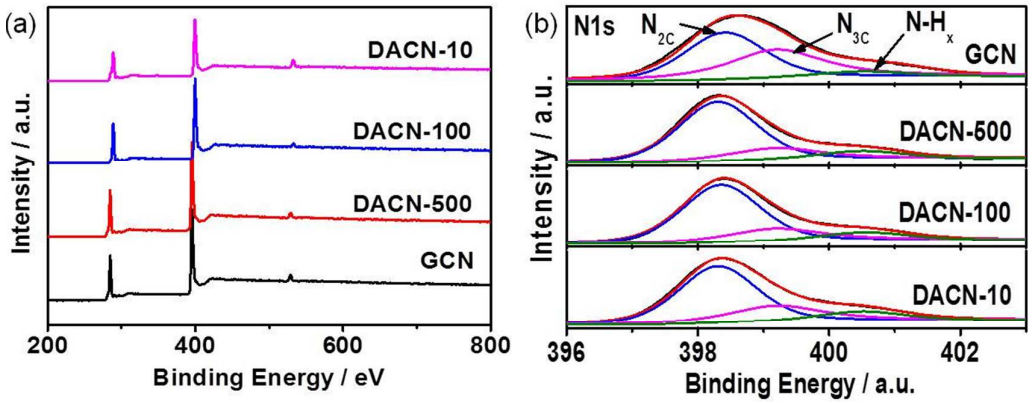

Figure S7. (a) XPS spectra and (b) the corresponding high-resolution N1s peak of GCN, DACN-500, DACN-100 and DACN-10.

Table S3. The element content (at%) of GCN, DACN-500, DACN-100 and DACN-10 determined by XPS.

Sample	C	N	O	C/N
GCN	**38.55**	**58.76**	**2.69**	**0.66**
DACN-500	**39.16**	**58.81**	**2.03**	**0.67**
DACN-100	**41.66**	**56.79**	**1.55**	**0.73**
DACN-10	**47.76**	**45.41**	**6.84**	**1.05**

Table S4. The relative percentages (at%) of the nitrogen and carbon species for GCN, DACN-500, DACN-100 and DACN-10 obtained from XPS.

Sample	N_{2C}	N_{3C}	N-NH_x	$(N_2)C(NH_2)$	C-C
GCN	**63.2**	**25.9**	**10.9**	**83.2**	**16.8**
DACN-500	**68.7**	**22.2**	**9.1**	**87.6**	**12.4**
DACN-100	**71.3**	**20.9**	**7.8**	**92.2**	**7.8**
DACN-10	**66.1**	**24.2**	**9.7**	**86.9**	**13.1**

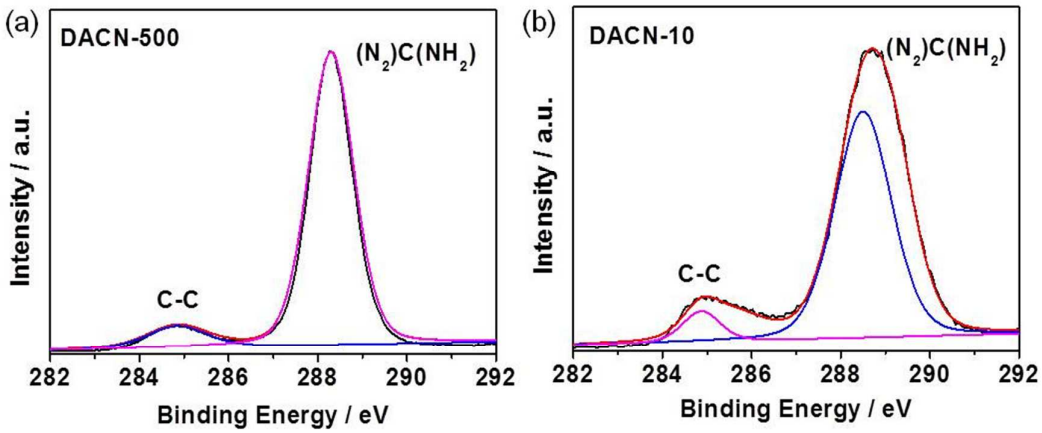

Figure S8. The corresponding high-resolution C1s peak of DACN-500 and DACN-10.

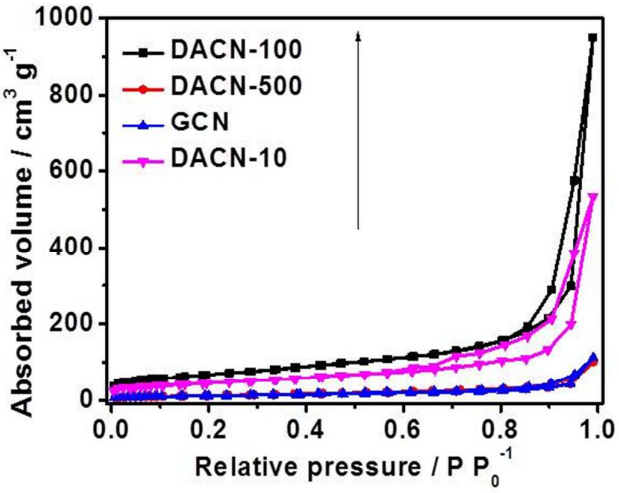

Figure S9. N_2 adsorption isotherms of GCN and DACN samples.

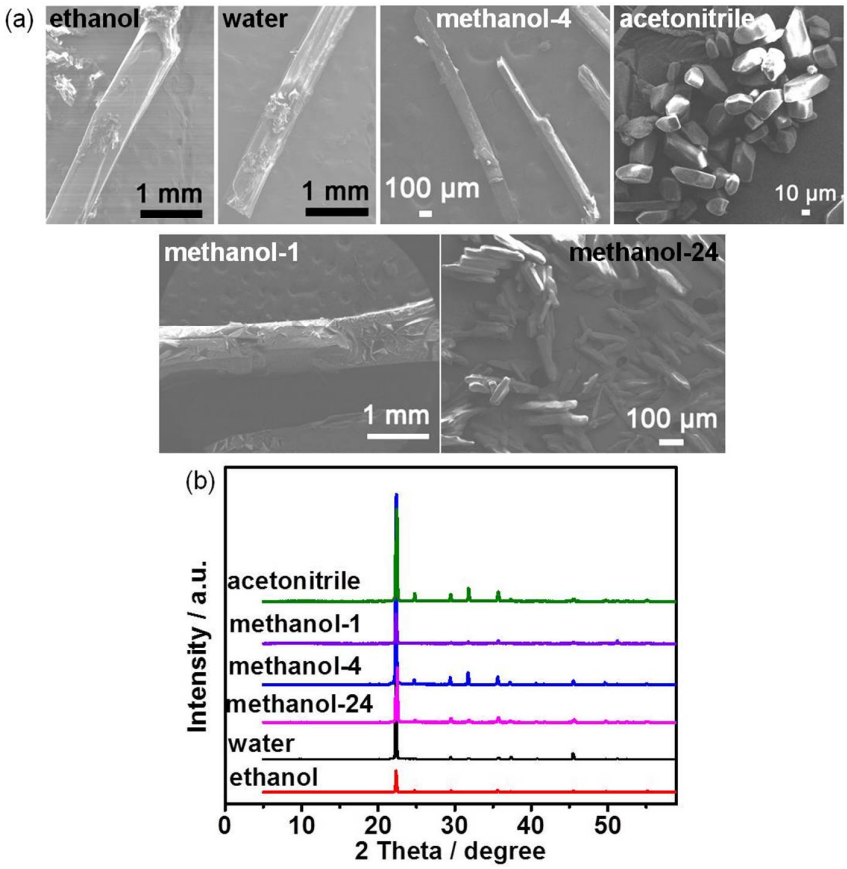

Figure S10. (a) SEM images, (b) XRD patterns of different urea crystals obtained from ethanol (U-ethanol), water (U-water), methanol (U-methanol-1, U-methanol-4 and U-methanol-24) and acetonitrile (U-acetonitrile), respectively. c) Photocatalytic activities of DACN samples derived from ethanol (U-ethanol-derived DACN), water

(U-water-derived DACN), methanol (U-methanol-1-derived DACN, U-methanol-4-derived DACN and U-methanol-24-derived DACN) and acetonitrile (U-acetonitrile-derived DACN), respectively.

To explain the size effect for the enhanced photocatalytic activities further, various urea crystals with different forms, morphologies and particle sizes were obtained from different solvents. Compared with pristine urea (Figure 2a), the U-ethanol shows a larger grain size, while others exhibit smaller grain size (Figure S10a). In addition, these urea crystals size is decreased in this order: U-ethanol＞pristine urea＞U-water ＞U-methanol＞U-acetonitrile. The urea grains with different sizes display different XRD peak intensity (Figure S10b), because of their various morphologies with exposed face in varying degrees. It is well to be reminded that the photocatalytic hydrogen evolution activities increase with the decreasing of the urea crystals size in the following order (Figure 5b): U-ethanol-derived DACN (3920 μmol h^{-1} g^{-1})＜GCN (4365 μmol h^{-1} g^{-1}) ＜ U-water-derived DACN (6407 μmol h^{-1} g^{-1}) ＜ U-methanol-4-derived DACN (16071 μmol h^{-1} g^{-1})＜U-acetonitrile-derived DACN (22577 μmol h^{-1} g^{-1}). In addition, the HER of U-methanol-4-derived DACN (16071 μmol h^{-1} g^{-1}) is smaller than that of DACN-500 (19280 μmol h^{-1} g^{-1}), and the HER of U-acetonitrile-derived DACN (22577 μmol h^{-1} g^{-1}) is lower than that of DACN-100 (37480 μmol h^{-1} g^{-1}) but higher than that of DACN-10 (17545 μmol h^{-1} g^{-1}, Figure 5a). The grain size of U-methanol-4 is larger than SRU-500, however, the size of U-acetonitrile is smaller than the SRU-100 but larger than SRU-10 (Figure S10a, Figure S5g and Figure 2c). From the results above, it can be concluded that the alternative explanations (i.e. impurity or one added during the recrystallization) for the enhanced photocatalytic activities are ruled out, and the precursor size is the real reason for the significantly improved catalytic properties. Similarly, the photocatalytic hydrogen evolution activities increase with the decreasing of the urea crystals size in this order: U-methanol-1-derived DACN (1864 μmol h^{-1} g^{-1})＜U-methanol-4-derived DACN (16071 μmol h^{-1} g^{-1})＜U-methanol-24-derived DACN (29790 μmol h^{-1} g^{-1}). Better yet, the HER of U-methanol-1-derived DACN (1864 μmol h^{-1} g^{-1}) is lower than

that of U-ethanol-derived DACN (3920 μmol h^{-1} g^{-1}), the HER of U-methanol-24-derived DACN (29790 μmol h^{-1} g^{-1}) is higher than that of U-acetonitrile-derived DACN (22577 μmol h^{-1} g^{-1}) but lower than that of DACN-100 (37480 μmol h^{-1} g^{-1}, Figure 5a). However, looking more closely, it was clear that the grain size of U-methanol-1 is larger than U-ethanol, the grain size of U-methanol-24 is larger than SRU-100, suggesting the photocatalytic performance increases with the decreasing of the urea crystals size (Figure S10a, Figure S5 and Figure 2c). Although the grain size of SRU-100 is larger than U-acetonitrile, the HER of DACN-100 is better than that of U-acetonitrile-derived DACN, further demonstrating the precursor size has a significant effect on the performance of the final DACN products.

Table S5. Summary of GCN-based photocatalysts for hydrogen evolution rate (HER) and apparent quantum efficiency (AQE).

Samples[a]	HER μmol h^{-1}	HER μmol h^{-1} g^{-1}	AQE	ref
DACN-100	1874 (50 mg)	37480	34.4 (400 nm) 31.9 (420 nm)	This work
UGCNPs	68.3 50 mg	1365	3.6 (420 nm)	s1
$LCN_{180\text{-}96}$	6.1 (50 mg)	122	N/A	s2
HCNS	224 (50 mg)	4480	7.5 (420 nm)	s3
NS-g-C_3N_4	574 (40 mg)	14350	9.6 (420)	s4
PCN	18.8 (4.69 mg)	401	N/A	s5
HR-CN	74 (20 mg)	3700	N/A	s6
g-C_3N_4 nanosheets[1]	93 (50 mg)	1860	3.75 (420 nm)	s7
g-C_3N_4 nanosheets[2]	*ca.* 33 (50 mg)	650	N/A	s8
HGCN	82.9 (10 mg)	8290	N/A	s9
mpg-C_3N_4	149 (1000	149	N/A	s10

	mg)			
PTI nanosheets	3.5 (2 mg)	1750	1.3 (400 nm)	s11
IGCNSs	44.5 (50 mg)	890	3.0 (420 nm)	s12
CNUB	278 (50 mg)	5560	N/A	s13
ACN	7.85 (50mg)	157.9	N/A	s14
CN-NS	*ca.* 310 (50mg)	*ca.* 6200	N/A	s15
PCN-S	79.8 (50mg)	1596	3.56 (420 nm)	s16
Urea-based g-C_3N_4	388.24 (20mg)	19412	26.5 (400 nm)	s17
monolayer nanomesh	85.1 (10 mg)	8510	5.1 (420 nm)	s18
"seaweed"	99 (10 mg)	9900	7.8 (420 nm)	s19
P-TCN	67 (100 mg)	670	5.68 (420 nm)	s20
g-C_3N_x	69 (10 mg)	6900		s21

[a] The photocatalysts listed in Table S5 were loaded with 3 wt% Pt co-catalyst; 10 vol% triethanolamine scavenger in an aqueous solution, excepting PCN which was loaded with 1 wt% Pt co-catalyst, 65 vol% triethanolamine scavenger in an aqueous solution, ACN was loaded with 6 wt% Pt co-catalyst, PCN-S which was loaded with 1 wt% Pt co-catalyst, 20 vol% triethanolamine scavenger in an aqueous solution. HER rates for external samples were measured by using a $\lambda \geq 420$ nm long-pass filter either, except Urea-based g-C_3N_4, which was measured by using a $\lambda \geq 400$ nm long-pass filter either. N/A= no applicable.

References

1. Han, Q.; Zhao, F.; Hu, C. G.; Lv, L. X.; Zhang, Z. P.; Chen, N. Qu, L. T. Facile Production of Ultrathin Graphitic Carbon Nitride Nanoplatelets for Efficient Visible-Light Water Splitting. *Nano Res*., **2015**, *8*, 1718–1728.
2. Cui, Y. J.; Ding, Z. X.; Fu, X. Z.; Wang, X. C. Construction of Conjugated Carbon Nitride Nanoarchitectures in Solution at Low Temperature for Photoredox Catalysis. *Angew. Chem. Int. Ed.*, **2012**, *51*, 11814–11818.
3. Sun, J. H.; Zhang, J. S.; Zhang, M. W.; Antonietti, M.; Fu, X. Z.; Wang, X. C. Bioinspired Hollow Semiconductor Nanosheets as Photosynthetic Nanoparticles. *Nat. Commun.*, **2012**, *3*, 1139–1145.
4. Zhang, J. S.; Zhang, M. W.; Yang, C.; Wang, X. C. Nanospherical Carbon Nitride Frameworks with Sharp Edges Accelerating Charge Collection and Separation at A Soft Photocatalytic Interface. *Adv. Mater.* **2014**, *26*, 4121–4126.
5. Hong, J.; Yin, S.; Pan, Y.; Han, J.; Zhou, T.; Xu, R. Porous Carbon Nitride Nanosheets for Enhanced Photocatalytic Activities. *Nanoscale*, **2014**, *6*, 14984–14990.
6. Zheng, Y.; Lin, L. H.; Ye, X. J.; Guo, F. S.; Wang, X. C. Helical Graphitic Carbon Nitrides with Photocatalytic and Optical Activities. *Angew. Chem. Int. Ed*., **2014**, *53*, 11926–11930.
7. Yang, S. B.; Gong, Y. J.; Zhang, J. S.; Zhan, L.; Ma, L. L.; Fang, Z. Y.; Vajtai, R.; Wang, X. C.; Ajayan, P. M. Exfoliated Graphitic Carbon Nitride Nanosheets as Efficient Catalysts for Hydrogen Evolution Under Visible Light. *Adv. Mater.*, **2013**, *25,* 2452–2457.
8. Niu, P.; Zhang, L.; Liu, G.; Cheng, H. M. Graphene-Like Carbon Nitride Nanosheets for Improved Photocatalytic Activities. *Adv. Funct. Mater.*, **2012**, *22*, 4763–4770.
9. Liang, Q. H.; Li, Z.; Huang, Z. H.; Kang, F. Y.; Yang, Q. H. Holey Graphitic Carbon Nitride Nanosheets with Carbon Vacancies for Highly Improved Photocatalytic Hydrogen Production. *Adv. Funct. Mater*., **2015**, *25*, 6885–6892.
10. Wang, X.; Maeda, K.; Chen, X.; Takanabe, K.; Domen, K.; Hou, Y.; Fu, X.;

Antonietti, M. Polymer Semiconductors for Artificial Photosynthesis: Hydrogen Evolution by Mesoporous Graphitic Carbon Nitride with Visible Light. *J. Am. Chem. Soc.*, **2009**, *131*, 1680–1681.

11. Schwinghammer, K.; Mesch, M. B.; Duppel, V.; Ziegler, C.; Senker, J.; Lotsch. B. V. Crystalline Carbon Nitride Nanosheets for Improved Visible-Light Hydrogen Evolution. *J. Am. Chem. Soc.*, **2014**, *136,* 1730–1733.
12. Han, Q.; Hu, C. G.; Zhao, F.; Zhang, Z. P.; Chen, N.; Qu, L. T. One-Step Preparation of Iodine-Doped Graphitic Carbon Nitride Nanosheets as Efficient Photocatalysts for Visible Light Water Splitting. *J. Mater. Chem. A*, **2015**, *3*, 4612–4619.
13. Lin, Z. Z.; Wang, X. C. Nanostructure Engineering and Doping of Conjugated Carbon Nitride Semiconductors for Hydrogen Photosynthesis. *Angew. Chem. Int. Ed.*, **2013**, *52*, 1735–1738.
14. Kang, Y.; Yang, Y.; Yin, L.; Kang, X.; Liu, G.; Cheng. H. M. An Amorphous Carbon Nitride Photocatalyst with Greatly Extended Visible-Light-Responsive for Photocatalytic Hydrogen Generation. *Adv. Mater.*, **2015**, *27*, 4572–4577.
15. Liu, G. G.; Wang, T.; Zhang, H. B.; Meng, X. G.; Hao, D.; Chang, K.; Li, P.; Kako, T.; Ye, J. H. Nature-Inspired Environmental "Phosphorylation" Boosts Photocatalytic H_2 Production over Carbon Nitride Nanosheets under Visible-Light Irradiation. *Angew. Chem. Int. Ed.* **2015**, *54*, 13561-13565.
16. Ran, J. R.; Ma, T. Y.; Gao, G. P.; Du, X. W.; Qiao, S. Z. Porous P-Doped Graphitic Carbon Nitride Nanosheets for Synergistically Enhanced Visible-Light Photocatalytic H_2 Production. *Energy Environ. Sci.*, **2015**, *8*, 3708–3717.
17. Martin, D. J.; Qiu, K. P.; Shevlin, S. A.; Handoko, A. D.; Chen, X. W.; Guo, Z. X.; Tang, J. W. Highly Efficient Photocatalytic H_2 Evolution from Water using Visible Light and Structure-Controlled Graphitic Carbon Nitride. *Angew. Chem. Int. Ed.*, **2014**, *53*, 9240–9245.
18. Han, Q.; Wang, B.; Gao, J.; Cheng, Z. H.; Zhao, Y.; Zhang, Z. P.; Qu, L. T. Atomically Thin Mesoporous Nanomesh of Graphitic C_3N_4 for High-Efficiency Photocatalytic Hydrogen Evolution. *ACS Nano*, **2016**, *10*, 2745–2751.

19. Han, Q.; Wang, B.; Zhao, Y.; Hu, C. G.; Qu, L. T. A Graphitic-C_3N_4 "Seaweed" Architecture for Enhanced Hydrogen Evolution. *Angew. Chem. Int. Ed*., **2015**, *54*, 11433–11437.
20. Guo, S.; Deng, Z. P.; Li, M. X.; Jiang, B. J.; Tian, C. G.; Pan, Q. J.; Fu, H. G. Phosphorus-Doped Carbon Nitride Tubes with a Layered Micro-nanostructure for Enhanced Visible-Light Photocatalytic Hydrogen Evolution. *Angew. Chem. Int. Ed.*, **2016**, *55*, 1830–1834.
21. Yu, H. J.; Shi, R.; Zhao, Y. X.; Bian, T.; Zhao, Y. F.; Zhou, C.; Waterhouse, G. I. N.; Wu, L. Z.; Tung, C. H.; Zhang, T. R. Alkali-Assisted Synthesis of Nitrogen Deficient Graphitic Carbon Nitride with Tunable Band Structures for Efficient Visible-Light-Driven Hydrogen Evolution. *Adv. Mater*., **2017**, *29*, 1605148.